

Interface Modification of Bernal- and Rhombohedral-Stacked Trilayer-Graphene/Metal Electrode on Resistive Switching of Silver Electrochemical Metallization Cells

Jer-Chyi Wang,^{*,†,‡,§} Ya-Ting Chan,[†] Wei-Fan Chen,[†] Ming-Chung Wu,^{||} and Chao-Sung Lai^{*,†,⊥,#}

[†]Department of Electronic Engineering and ^{||}Department of Chemical and Materials Engineering, Chang Gung University, Guishan Dist., 33302 Taoyuan, Taiwan

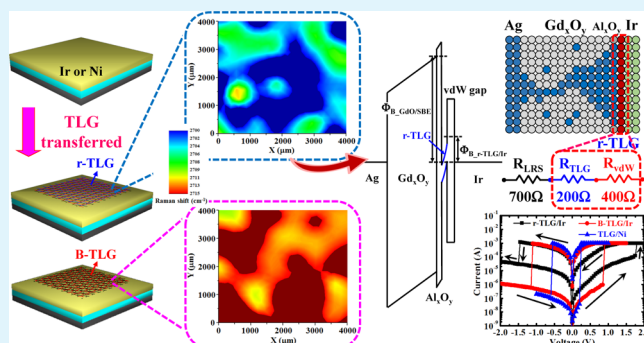
[‡]Department of Neurosurgery and [⊥]Department of Nephrology, Chang Gung Memorial Hospital, Linkou, Guishan Dist., 33305 Taoyuan, Taiwan

[§]Department of Electronic Engineering and [#]Department of Materials Engineering, Ming Chi University of Technology, Taishan Dist., 24301 New Taipei City, Taiwan

S Supporting Information

ABSTRACT: Bernal- and rhombohedral-stacked trilayer graphene (B- and r-TLG) on nickel (Ni) and iridium (Ir) films acting as bottom electrodes (BEs) of silver electrochemical metallization cells (Ag-EMCs) have been investigated in this study. Prior to the fabrication of the EMC devices, Raman mapping and atomic force microscopy are applied to identify the B- and r-TLG sheets, with the latter revealing a significant D peak and a rough surface for the Ir film. The Ag-EMCs with the stacked BE of r-TLG on the Ir film show a conductive mechanism of Schottky emission at the positive top electrode bias for both high- and low-resistance states that can be examined by the resistance change with the device area and are modulated by pulse bias operation. Thus, an effective electron barrier height of 0.262 eV at the r-TLG and Ir interface is obtained because of the conspicuous energy gap of r-TLG on the Ir film and the van der Waals (vdW) gap between the r-TLG and Ir contact metal. With the use of Ni instead of Ir contact metal, the Ag-EMCs with TLG BE demonstrate +0.3 V/−0.75 V operation voltages, more than 10⁴ s data retention at 115 °C and 250 times endurance testing, making the TLG sheets suitable for low-power nonvolatile memory applications on flexible substrates.

KEYWORDS: Bernal-stacked trilayer graphene (B-TLG), rhombohedral-stacked TLG (r-TLG), electrochemical metallization cell (EMC), van der Waals (vdW) gap, Schottky emission, nickel (Ni), iridium (Ir), gadolinium oxide (Gd_xO_y)



INTRODUCTION

To fulfill the high-density and low-power requirements, lateral and vertical device scaling has become an inevitable approach in the design of future floating-gate (FG) flash memory. Nevertheless, a significant gate leakage current of the vertically scaled FG flash memory can be observed from the ultrathin tunneling oxide (TO) layer in the subnanometer region.¹ In addition, the laterally scaled memory devices suffer from significant reliability degradations because of the FG–FG capacitive coupling among the neighboring memory cells.² To overcome these issues, some promising candidates have been proposed to replace the FG flash memory in future nonvolatile memories (NVMs); in particular, resistive random access memory (RRAM) has been extensively investigated.^{3–5} The RRAM, which is composed of a resistive switching (RS) layer and two metal electrodes, can repeatedly change the conductivity of the RS layer between the high-resistance state

(HRS) and the low-resistance state (LRS) by the sweep or pulse voltage operation. It is reported that high-*k* materials such as TaO_x,⁶ HfO₂,⁷ and Gd_xO_y⁸ can be used as the RS layer to exhibit a bistable RS behavior. The RS process involves the formation and rupture of conductive filaments (CFs) within the RS layer by oxygen vacancies or cations induced by different polarities of the electric field.⁹ The bulk-dominated RS of the cation CFs in the RS layer, also called the solid electrolyte, has been considered as the electrochemical metallization cell (EMC) or the conductive bridge RAM.^{10,11} The active silver (Ag), copper (Cu), and nickel (Ni) electrodes have been examined for the electrochemically RS layer.^{11–13} Compared to the conventional RRAMs, the EMCs have attracted much

Received: July 17, 2017

Accepted: September 29, 2017

Published: September 29, 2017

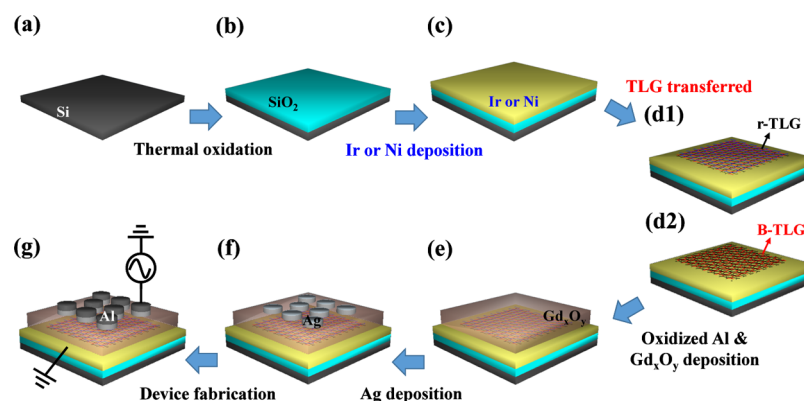


Figure 1. Fabrication procedures of the Ag-EMCs with different SBES of TLG on the contact metals. (a) n-type Si(100) wafers with standard RCA clean, (b) thermally grown SiO_2 film, (c) physical-vapor-deposited Ir and Ni films, (d1) r-TLG transferred onto the Ir and Ni films, (d2) B-TLG transferred onto the Ir and Ni films, (e) thermally oxidized aluminum (Al) layer and sputtered Gd_2O_3 RS layer deposition, (f) Ag top electrode (TE) deposition, and (g) Al contact formation to fabricate the Ag-EMCs.

attention for their use in future NVM applications because of their advantages of low operation voltage, low programming current, high switching speed, and the feasibility of multibit storage.¹⁴

Recently, two-dimensional (2D) materials such as graphene, hexagonal boron nitride (h-BN), and transition metal dichalcogenides have attracted much attention because of their planar structure and outstanding properties.^{15–17} These materials have been integrated in various applications such as field-effect transistors (FETs), heterojunctions, NVMs, photo-detectors, supercapacitors, and conductive transparent electrodes.^{18–23} Graphene has been examined as the electrode of RRAMs, and some obvious properties have been addressed. By using the conventional wet transfer process of chemical vapor deposition (CVD) graphene with polymethyl methacrylate (PMMA) acting as the supporting layer,²⁴ it is easy to form cracks because of the imperfect contact with the target substrate, especially for the rough metal surface, which restricts the industrial scalability applications of the monolayer CVD graphene.^{24,25} The bilayer graphene (BLG) acting as the electrode of RRAMs can modify the switching window of a gate-controlled RRAM in situ owing to its unique band gap opening property,²⁶ making the low-power operation of RRAMs difficult. Though a multilayer graphene (MLG) with 14 layers has been inserted between the metal electrode and the RS layer for the reduction of power consumption of a RRAM because of the DOS-limited tunneling current between the graphene layers, the fabrication of a 14-layered MLG is too complicated to be used in NVMs.²⁷ Furthermore, an oxide-based resistive memory device with functionalized graphene electrodes offered an internal selector element for the suppression of the sneak path problem in passive crossbar arrays,²⁸ however, the operation voltages of the device increased significantly with a relatively small memory window. On the other hand, Bao et al. proposed the stacking-dependent band gap of trilayer graphene (TLG), where the Bernal-stacked TLG (B-TLG) is semimetallic with a band overlap and the rhombohedral-stacked TLG (r-TLG) is semiconducting with a tunable band gap,²⁹ resulting in a Schottky interface with a van der Waals (vdW) gap between the r-TLG and the metal electrodes except for the case of the Ni electrode.^{30,31} However, the effects of different stacked TLG and metal electrodes on the RS of RRAMs have not been investigated to date. In this study, the characteristics of the Ag-EMCs with stacked bottom

electrodes (SBES) of B- and r-TLG on the iridium (Ir) and Ni films are investigated. The material natures of B- and r-TLG on the Ir and Ni films are identified by Raman mapping and atomic force microscopy (AFM) images. By analyzing the conductive mechanisms at different bias polarities and the resistance values under different pulse frequencies, the energy band structures and RS mechanisms of the Ag-EMCs with SBES of B- and r-TLG on the Ir and Ni films are proposed, demonstrating the specific memory behaviors for future applications of 2D materials in NVMs.

EXPERIMENTAL SECTION

Sample Preparation. The Ag-EMC devices with SBES of B- and r-TLG on the Ir and Ni films were prepared on n-type Si(100) wafers. The wafers were first cleaned using the standard Radio Corporation of America (RCA) cleaning procedure. Then, a 300 nm thick SiO_2 layer was grown as the isolation layer on the Si wafers by using a horizontal furnace at 1000 °C. After that, some samples were subjected to sputtering in a cylindrical dc sputtering chamber for iridium (Ir) contact metal deposition. Prior to the deposition, the background pressure of the system was pumped down to 10^{-5} Torr, and a 3 in. diameter Ir target was pre-cleaned using argon plasma for 10 min to remove the native surface oxides. Next, a 50 nm thick Ir layer was deposited via dc sputtering at 20 mTorr with an argon gas flow of 25 sccm. In addition, some samples were deposited using a thermal evaporator at 10^{-6} Torr with a pure Ni bullet (99.99% purity) to form a 50 nm thick Ni contact metal layer. After the formation of the contact metals, the CVD graphene was transferred three times onto the metal films to obtain the TLG. The samples with the SBES of B- and r-TLG on the Ir contact metal are labeled as B-TLG/Ir and r-TLG/Ir, respectively. As a result of the good contact behavior of TLG on Ni films,^{30,31} the electrical characteristics of the samples with SBES of r-TLG and B-TLG on the Ni contact metal are the same, which will be presented later. Thus, these samples are labeled as TLG/Ni. Prior to the deposition of the RS layer, we use a thermally oxidized aluminum (Al) layer (Al_2O_3) to protect the TLG from plasma damage during the rf sputtering.³² Subsequently, all samples were deposited using rf sputtering at a pressure of 10 mTorr to obtain a 30 nm thick Gd_2O_3 RS layer. Then, a 40 nm thick Ag film was deposited by a thermal evaporator at 10^{-6} Torr with a pure Ag bullet (99.99% purity) as the top electrode (TE). Finally, a 300 nm thick Al film was also deposited by a thermal evaporator at 10^{-6} Torr with a pure Al bullet (99.999% purity) on the Ag TE to serve as the contact metal, thus avoiding the probing issue of such a thin Ag film. Meanwhile, an area with a diameter of 0.01–0.04 cm was defined by the shallow mask. Figure 1 illustrates the entire fabrication process of the Ag-EMC devices with SBES of TLG on the contact metals.

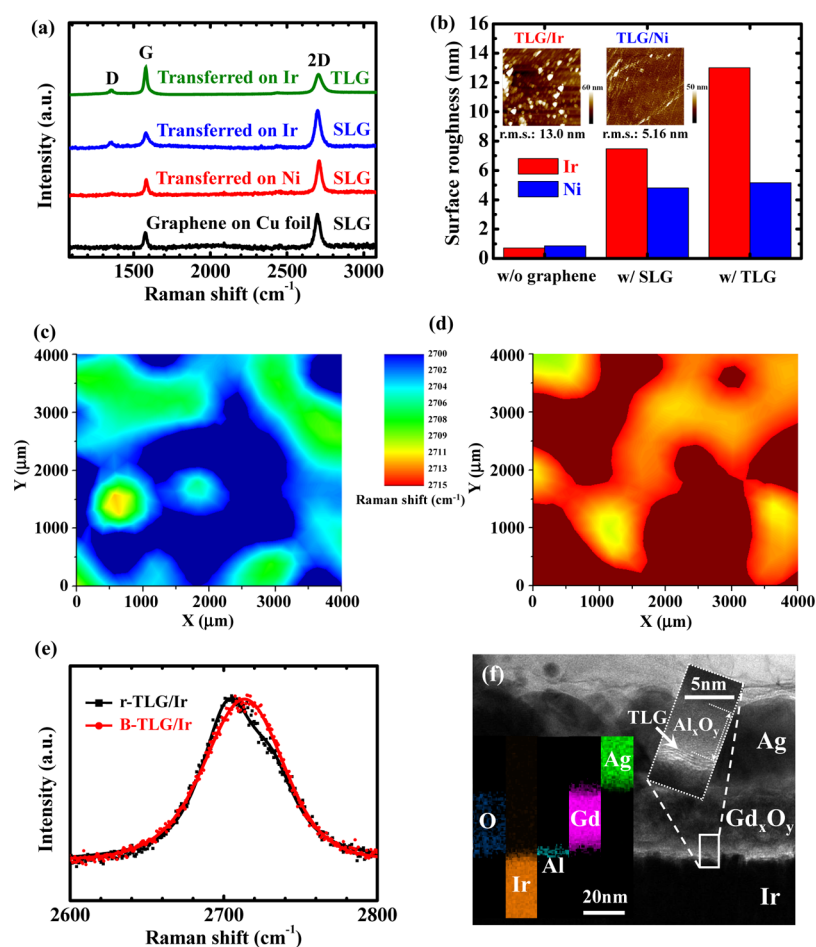


Figure 2. (a) Raman spectra of the single-layer graphene (SLG) grown on a copper foil and transferred onto the Ni and Ir films. (b) Bar chart of the surface roughness (rms) of the deposited Ni and Ir films and the SLG and TLG transferred onto the Ni and Ir films. The FE-SEM images of the TLG transferred onto the Ni and Ir films are shown in the inset figures. Raman mapping of the (c) B- and (d) r-TLG for the EMC device fabrication. The red and blue colors show the up- and downshifts of the Raman wavenumber. (e) Raman spectra of r- and B-TLG on the Ir film from (c) and (d). (f) Cross-sectional HRTEM image and EDX mapping of the Ag/Gd_xO_y/Al_xO_y/TLG/Ir structure on the SiO₂/Si substrate.

Characterization. Following the TLG formation, Raman mapping was used to confirm the stacked structures using an NT-MDT Raman microscopy system at 473 nm and a spot size of 1 μm . The mapping was performed with a rapid scanning of a 4 mm \times 4 mm area, acquiring 400 (20 \times 20) spectra, each with an integration time of 1 s. Because of the time delay between the acquisitions, the effective acquisition time was 2.75 s and the total acquisition time per image was 1100 s. With a minimal interval between frames, the experiments produced 800 (20 \times 20 \times 2) Raman spectra. Prior to the measurement, the Si peak at 520 cm^{-1} was used as a reference for calibration. Furthermore, single-layer graphene (SLG) layers deposited on a copper foil and transferred onto the Ir and Ni contact metals were examined by using Raman spectra to understand the contact behaviors of graphene and the metal films. In addition, a high-resolution transmission electron microscopy (HRTEM) image was obtained using an FEI Tecnai G2 F20 scanning transmission electron microscopy (STEM) system. The elemental composition image of the stacked Ag/Gd_xO_y/Al_xO_y/TLG/Ir structure taken by energy-dispersive X-ray spectroscopy (EDX) mapping of the STEM system was investigated. The surface morphology of graphene sheets transferred onto the metal films was examined using a Bruker AXS MultiMode 8 AFM system. The crystal structure was analyzed by an X-ray diffractometer (XRD) using a Bruker D2 phaser system with Cu K α radiation to understand the reaction of the Ni electrode with TLG sheets. For the device characterization, all samples were biased and measured using a Keithley 4200 semiconductor characterization

system. The voltage bias was applied on the Ag TE, and the BE was definitely grounded.

RESULTS AND DISCUSSION

Material Analyses of Stacked TLG on Metal Films.

Figure 2a shows the Raman spectra of SLG grown on a copper foil and the graphene sheets transferred onto the Ni and Ir films. The SLG grown on a copper foil and transferred onto the Ni film shows a typical signature for monolayer graphene with the 2D/G ratio close to 2.1. Nevertheless, for the SLG transferred onto the Ir film, a significant D peak can be observed. Notably, a decreased 2D/G ratio with an obvious D peak implies the presence of TLG on the Ir film. To further examine the graphene sheets on the metal films, the tapping-mode AFM images of SLG and TLG transferred onto the Ir and Ni films were investigated and are shown in Figures S1 and S2 of the Supporting Information, respectively. The topographic and phase images with the field of view of 10 μm \times 10 μm were collected simultaneously and are summarized in the plot of the surface roughness (rms) in Figure 2b. For the graphene sheets transferred onto the Ir film, the surface morphology of the stacked layers becomes extremely rough, which can be ascribed to the van der Waals gap (vdW) between graphene and the Ir film.³³ On the other hand, for the graphene sheets transferred onto the Ni film, a slightly rough surface is

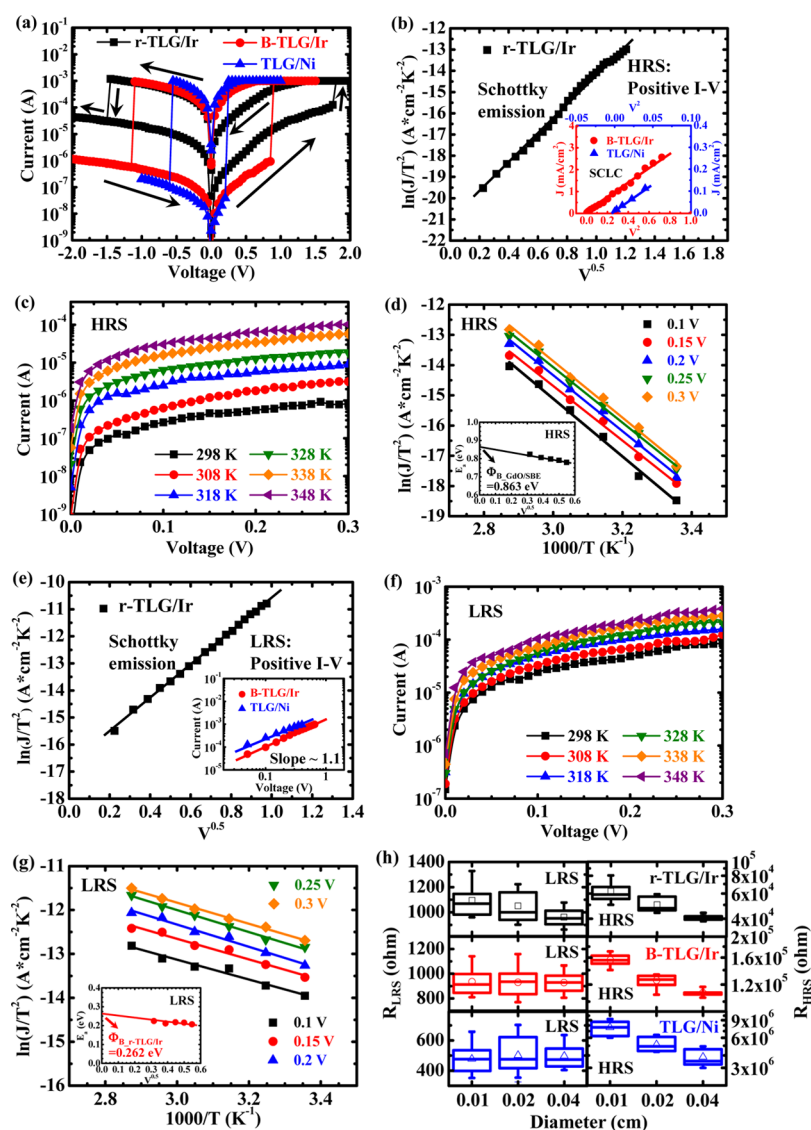


Figure 3. (a) Typical RS current–voltage (I – V) characteristics of the Ag-EMCs with different SBEs of TLG on the contact metals. (b) J/T^2 vs $V^{0.5}$ fitting of the r-TLG/Ir sample at the positive TE bias of the HRS. The inset shows J – V^2 fitting of the B-TLG/Ir and TLG/Ni samples. (c) Temperature dependence of I – V curves of the r-TLG/Ir sample at the positive TE bias of the HRS. (d) J/T^2 vs $1000/T$ fitting of the r-TLG/Ir sample at different TE biases. The inset shows the equivalent Schottky barrier height E_a vs $V^{1/2}$ curve. (e) J/T^2 vs $V^{0.5}$ fitting of the r-TLG/Ir sample at the positive TE bias of the LRS. The inset shows J – V fitting at logarithmic scales of the B-TLG/Ir and TLG/Ni samples. (f) Temperature dependence of I – V curves of the r-TLG/Ir sample at the positive TE bias of the LRS. (g) J/T^2 vs $1000/T$ fitting of the r-TLG/Ir sample at the positive TE bias of the LRS. The inset shows the E_a vs $V^{1/2}$ curve. (h) Area dependence of the resistance at the HRS and LRS of the Ag-EMCs with different SBEs of TLG on the contact metals.

observed because of the nonconformal alignment of graphene on the Ni film.³⁴ The hybridization between the contact metal's atoms and the graphene sheet is responsible for the smooth surface of SLG and TLG sheets on the Ni film,³¹ compared to those on the Ir film. The results of the significant D peak observed in Raman spectra and the rough film surface observed by AFM images of graphene sheets on the Ir film indicate the imperfect interface between graphene and the Ir film. After the transfer process, the Raman mapping of the 2D peak was performed to identify the B- and r-TLG for the subsequent device fabrication with the results shown in Figure 2c,d, respectively. The red and blue colors show the up- and downshifts of the Raman wavenumber, representing the ABA (Bernal) and ABC (rhombohedral) TLG stackings, respectively. The typical 2D peak of B- and r-TLG obtained from Raman mapping (Figure 2c,d) is shown in Figure 2e and is

similar to that proposed by Bao et al.²⁹ In particular, the 2D peaks of r- and B-TLG on the Ir film are slightly blue-shifted, which can be attributed to the p-type doping by oxygen ambient in the environment.³⁵ Then, the fabrication of Ag-EMCs with B- and r-TLG on the Ni and Ir contact metals was completed, where the RS layer is Gd_xO_y and the active TE metal is silver. Figure 2f presents the HRTEM image and the EDX mapping of the Ag/ Gd_xO_y / Al_xO_y /TLG/Ir structure on the SiO_2/Si substrate. An obvious TLG between the Al_xO_y and the Ir film is observed from an enlarged picture in the inset of this figure, and the elemental composition can be clearly identified from the EDX mapping. In addition, the thickness of the Al_xO_y film was found to be approximately 5 nm on the surface of TLG. To confirm if there is any reaction of the Ni electrode with TLG, the XRD patterns and Raman spectra were observed and are shown in Figure S3 of the Supporting

Information. The samples with and without baking in N₂ ambient at 200 °C for 4 h were investigated to understand the influence of heat generation from the following film deposition processes. The Ni films without any TLG sheet were also observed as a reference. From the XRD analysis, we can only observe the pure Ni signals for all samples. In addition, the Raman spectra of the samples with and without baking are quite similar. These results imply that there is no reaction of the Ni electrode with TLG.

Conductive Mechanisms. Figure 3a shows the typical RS current–voltage (*I*–*V*) characteristics of the Ag-EMCs with different SBEs of TLG on the contact metals. To operate the devices, a forming process is needed for the formation of a conductive pathway, as shown in Figure S4 of the Supporting Information. All samples show the bipolar RS behavior with set and reset operations at positive and negative TE biases, respectively. For the samples with an active metal electrode such as Ag, the electrochemical metallization theory can be used to explain the bipolar RS.¹¹ Interestingly, compared to the other samples, the r-TLG/Ir sample shows a notably different *I*–*V* behavior, with high set and reset voltages of 1.8 and –1.5 V, respectively. To understand the dominant conductive mechanism of the memories with different SBEs of TLG on the contact metals, the *I*–*V* characteristics of the samples at both bias polarities of the HRS and LRS are examined. Figure 3b depicts the current density divided by the square of the measured temperature (*J*/*T*²) as a function of the square root of the applied voltage (*V*^{0.5}) of the r-TLG/Ir sample at the positive TE bias of the HRS. The linear fit of the curve means that the dominant carrier transport mechanism of the r-TLG/Ir sample at the positive TE bias of the HRS is Schottky emission as expressed by the following equation:

$$J = A^*T^2 \times \exp\left(\frac{-q(\Phi_B - \sqrt{qV/4\pi\epsilon_s d})}{k_B T}\right) \quad (1)$$

where *A*^{*} is the Richardson constant, *T* is the absolute temperature, *k_B* is the Boltzmann constant, *q* is the electric charge, *V* is the TE bias, *ε_s* is the semiconductor permittivity, *d* is the thickness of the RS layer, and *Φ_B* is the barrier height between the semiconductor and the metal layer. For simplicity, we used the Richardson constant of *A*^{*} = 120 A·cm^{−2}·K^{−2} and the semiconductor permittivity of 16 and 3.0 for Gd_xO_y and TLG film, respectively.^{36,37} To obtain the Schottky barrier height (*Φ_B*_{GdO/SBE}) between the Gd_xO_y RS layer and the r-TLG/Ir SBE, the *I*–*V* characteristics of the r-TLG/Ir sample at the positive TE bias of the HRS were measured at elevated temperatures (Figure 3c), and the ln(*J*/*T*²) versus 1000/*T* curves at different TE biases are displayed in Figure 3d. With the extraction of the slope of the curves, the equivalent Schottky barrier height (*E_a* = −*q*[*Φ_B* − (*qV*/4*πε_s**d*)^{1/2}]) was obtained and the *E_a* versus *V*^{1/2} curve is plotted in the inset of this figure.³⁸ By extrapolating the curve to the *y*-axis, the barrier height of the Gd_xO_y/SBE interface can be determined to be 0.863 eV, which is similar to that of the Gd_xO_y/Pt interface.³⁹ Thus, the thin Al_xO_y film between the Gd_xO_y layer and the TLG presents a nearly negligible influence on the RS of the Ag-EMCs with different SBEs of the TLG on contact metals.⁴⁰ In addition, it can be observed that the *I*–*V* characteristics of the B-TLG/Ir and TLG/Ni samples at the positive TE bias of the HRS are well-fitted by the current density as a function of the square of the applied TE voltage (*J*–*V*²) characteristics, as shown in the inset of Figure 3b, implying that the space-charge-

limited-current (SCLC) conduction is the dominant carrier transport mechanism of these samples at the positive TE bias of the HRS. The r-TLG sheet with a band gap, which is between the Gd_xO_y RS layer and the Ir-BE, is responsible for the dominant carrier transport mechanism of Schottky emission for the r-TLG/Ir sample.²⁹ It is worth noticing that the *I*–*V* curve of the r-TLG/Ir sample at the positive TE bias of the HRS is different from that at the negative bias, as shown in Figure 3a. To confirm the conductive mechanism, the *I*–*V* characteristics at the negative TE bias of the HRS were also studied and are shown in Figure S5a of the Supporting Information. The results suggest that the data for all samples are well-fitted by the *J*–*V*² characteristics, indicating the SCLC conduction. On the other hand, at the LRS, the conductive mechanism for all samples at the negative TE bias is dominated by ohmic conduction (Figure S5b of the Supporting Information), which can be examined by the linear fitting of the logarithmic scales of the current versus absolute value of the TE voltage with a slope of approximately one. Furthermore, at the positive TE bias of the LRS in Figure 3a, the *I*–*V* curve of the r-TLG/Ir sample appears to differ from the other curves, indicating the presence of Schottky emission as examined in Figure 3e. According to eq 1, the barrier height of the r-TLG/Ir interface, *Φ_B*_{r-TLG/Ir} which can be obtained at the positive TE bias of the LRS by examining the *I*–*V* characteristics at elevated temperatures (Figure 3f), extracting the slope of the curves of ln(*J*/*T*²) versus 1000/*T* at different TE biases, and extrapolating the curve of *E_a* versus *V*^{1/2} to the *y*-axis (Figure 3g), is determined to be 0.262 eV. This value is larger than the energy gap of 0.009–0.023 eV of the suspended r-TLG obtained by directly probing with scanning tunneling microscopy (STM)⁴¹ and roughly the same as the energy gap of 0.1–0.3 eV of the r-TLG on metals obtained using the density functional theory with dispersion correction.⁴² The large Schottky barrier height of the r-TLG/Ir interface can be ascribed to the presence of a vdW gap between the r-TLG and the Ir electrode.³⁰ The conductive mechanisms of the Ag-EMCs with different SBEs of TLG on the contact metals can be further examined by the area dependence of the resistance at the HRS and LRS, as shown in Figure 3h. At the HRS, all samples present the decrease of resistance with the increase of the device area, indicating the Schottky emission or SCLC. On the other hand, at the LRS, only the r-TLG/Ir sample shows the area dependence of the resistance. The conductive mechanisms of all samples at positive and negative TE biases of the HRS and LRS are summarized in Table S1 of the Supporting Information. In this table, the conductive mechanisms of the r-TLG/Ir sample at positive and negative TE biases of the LRS are Schottky emission and ohmic conduction, respectively, revealing the diode operation of the r-TLG and Ir junction, as shown in Figure S6a of the Supporting Information. Besides, the B-TLG/Ir and TLG/Ni samples with ohmic conduction at both bias polarities of the LRS demonstrate the ohmic operation of the junctions (Figure S6b of the Supporting Information).

Energy Band Diagrams and RS Mechanisms. Figure 4a presents the statistical distributions of the operation voltages, resistances at the HRS and LRS, and the resistance ratio of the Ag-EMCs with different SBEs of TLG on the contact metals. In this figure, the r-TLG/Ir sample shows higher operation voltages and a lower resistance value at the HRS than those for the other samples, contributing to a low resistance ratio of less than 10². Furthermore, for the B-TLG/Ir sample, the operation voltages and the resistances at the HRS and LRS are close to

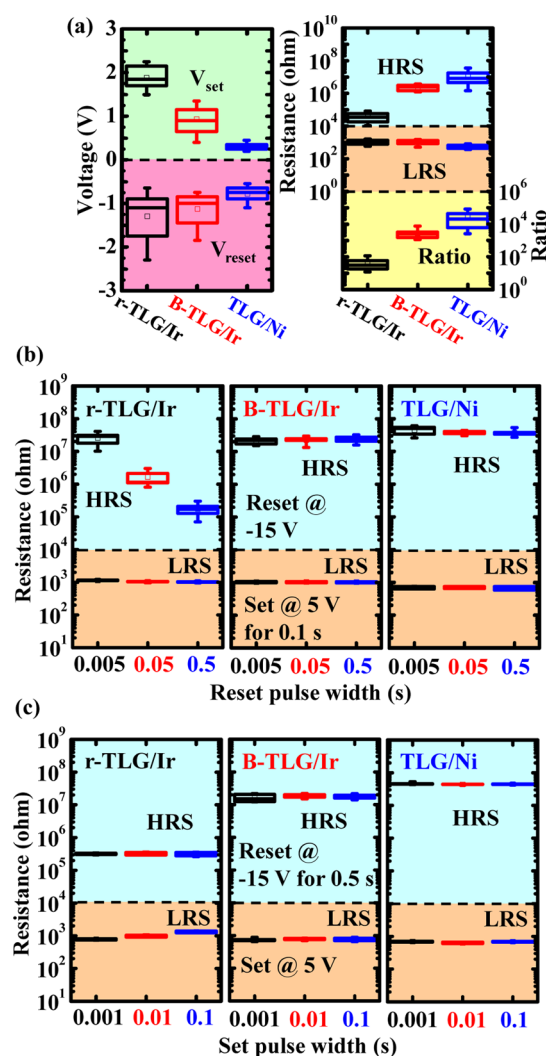


Figure 4. (a) Statistical distributions of the operation voltages, resistances at the HRS and LRS, and the resistance ratio of the Ag-EMCs with different SBEs of TLG on the contact metals. With different (b) reset and (c) set pulse operations, the statistical distributions of the resistances at the HRS and LRS of all samples are also examined. The set pulse is 5 V for 0.001–0.1 s, and the reset pulse is –15 V for 0.005–0.5 s.

the values of the TLG/Ni sample, indicating similar electrical behaviors and conductive mechanisms as shown in Figure 3. The operation currents, voltages, and powers of all samples at set and reset processes can be obtained from Figure 3a and are summarized in Table S2 of the Supporting Information. It can be observed that the operation power of the TLG/Ni sample at a set process is 7.72 nW, which is much lower than that of the r-TLG/Ir and B-TLG/Ir samples. The memory devices without TLG sheets were also investigated and have been proposed in our previous work.⁴³ The memory with Ir-BE, labeled as Ir, showed a Schottky-emission-dominated RS at the interface between the Ir-BE and the RS layer, whereas the sample with Ni-BE, labeled as Ni, demonstrated a cation-dominated RS behavior within the Gd_xO_y/Al_xO_y layer. The typical I – V characteristics and the statistical distributions of the operating voltages, resistances at the HRS and LRS, and the resistance ratio of the samples with Ir- and Ni-BEs are shown in Figure S7 of the Supporting Information. Compared to the samples without TLG sheets, the operation voltages of the r-TLG/Ir and B-TLG/Ir samples increase dramatically while those of the TLG/Ni sample decrease significantly. The Schottky interface with a van der Waals (vdW) gap between the r-TLG and the Ir-BE is responsible for the increase of the operation voltages of the r-TLG/Ir sample, leading to the drift of Ag ions into the RS layer for the lower resistance at the HRS. For the TLG/Ni sample, the rough surface of TLG on the Ni film (Figure 2b) induces a locally high electric field of the RS layer for the help of the formation of Ag-CF,⁴⁴ contributing to the reduced operation voltages and a lower resistance value at the HRS compared to those of the Ni sample. Figure 4b,c shows the statistical distributions of the resistances at the HRS and LRS with pulse operation for all samples. The set pulse is 5 V for 0.001–0.1 s, and the reset pulse is –15 V for 0.005–0.5 s. Generally, there is no pulse width dependence of the resistance values at either HRS or LRS, which can be observed in the B-TLG/Ir and TLG/Ni samples shown in Figure 4b,c. On the other hand, for the r-TLG/Ir sample, the decrease of the reset and set pulse width results in an increase of the resistance at the HRS and a decrease of the resistance at the LRS, respectively, approaching the resistance values of the other two samples and achieving a large resistance ratio. The change of the resistance value with different set and reset pulse widths of the r-TLG/Ir sample is due to the existence of a diode at the r-TLG and Ir junction, that is, the Schottky barrier, as discussed in Figure 3,

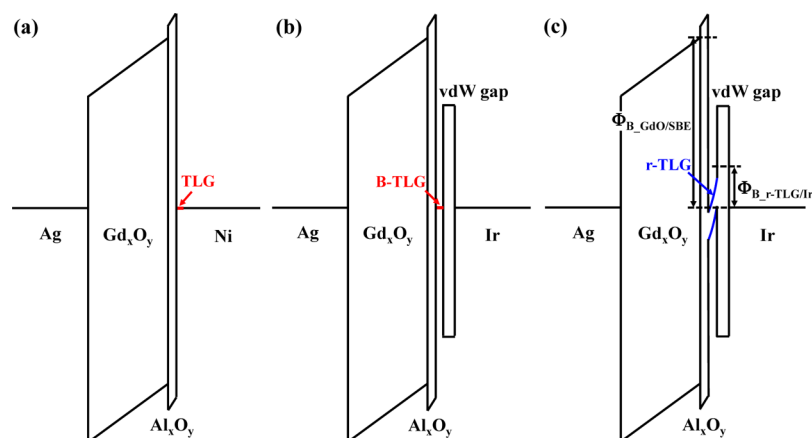


Figure 5. Energy band diagrams of the (a) TLG/Ni sample, (b) B-TLG/Ir sample, and (c) r-TLG/Ir sample. The effective electron barrier height of the Gd_xO_y /SBE ($\Phi_{B_GdO/SBE}$) and the r-TLG/Ir interface ($\Phi_{B_r-TLG/Ir}$) was found to be 0.863 and 0.262 eV, respectively.

which blocks the influence of the low-frequency set and reset pulse biases. The energy band diagrams of the Ag-EMCs with different SBEs of TLG on the contact metals are shown in Figure 5a–c. It is important to note that the energy band diagram of TLG changes according to the stacking-dependent TLG and interface-correlated contact metals.^{29,30} This gives rise to a vdW gap between the TLG and the Ir film and a significant energy band gap of r-TLG as shown in Figure 5b,c, leading to the asymmetric I – V characteristics and pulse-bias-dependent resistance values of the r-TLG/Ir sample, as discussed in Figures 3 and 4. Furthermore, the effective electron barrier height of the Gd_xO_y /SBE ($\Phi_{\text{B-GdO/SBE}}$) and r-TLG/Ir interface ($\Phi_{\text{B-r-TLG/Ir}}$) derived from eq 1 was found to be 0.863 and 0.262 eV, respectively, as marked in Figure 5c.

Traditionally, the electrochemical metallization theory has been proposed to explain the set and reset operations of the EMCs with the solid electrolyte materials of high solubility and diffusion coefficient of metal ions.⁴⁵ The metal dissolution, drift, nucleation, and growth reactions are suggested under a specific bias voltage on the electrode. To prove the formation of the cation filament, the temperature dependence of the resistance values at the LRS of the TLG/Ni sample is presented in Figure S8 of the Supporting Information. The increase of the resistance value at the LRS with the increase of the measurement temperature indicates that the conductive species should be metal ions. According to the temperature coefficient of the resistance value at the LRS of $3.98 \times 10^{-3} \text{ K}^{-1}$, which is similar to the value of $3.80 \times 10^{-3} \text{ K}^{-1}$ for pure Ag at 293 K,⁴⁶ the conductive species of the TLG/Ni sample are Ag ions. For the Ag-EMCs with different SBEs of TLG on the contact metals, the RS mechanisms are proposed and illustrated in Figure 6. After the formation process, lots of Ag ions can easily capture electrons and then reduce back to Ag atoms in $\text{Gd}_x\text{O}_y/\text{Al}_x\text{O}_y$ films to form a conductive pathway with the narrowest part connecting the Ag TE (Figure 6b,e,h), leading to the LRS. The resistance at the LRS (R_{LRS}) of the Ag-EMCs should be roughly 700 Ω , which can be obtained from the mean value of the resistance at the LRS of the TLG/Ni sample (Figure 4a). In addition, because of the presence of a vdW gap between the TLG and the Ir film of the B-TLG/Ni sample (Figure 5b), the resistance of the vdW gap (R_{vdW}) can be obtained as 400 Ω by calculating the additional resistance value at the LRS of the B-TLG/Ir sample compared to that of the TLG/Ni sample. Moreover, comparing the resistance value at the LRS between the B-TLG/Ir and r-TLG/Ir samples, it is observed that the resistance of the r-TLG film with a significant energy band gap (R_{TLG}) (Figure 5c) is approximately 200 Ω . The equivalent circuit diagrams of resistance for the Ag-EMCs with different SBEs of TLG on the contact metals at the LRS are illustrated in Figure 6c,f,i. By applying a negative TE bias, the Ag filaments within the $\text{Gd}_x\text{O}_y/\text{Al}_x\text{O}_y$ films are dissolved and are returned to the Ag TE, contributing to the HRS. Because of the reset voltage drop on the vdW gap and r-TLG film, the Ag-CF dissolution efficiency of the B-TLG/Ir and r-TLG/Ir samples decreases, as shown in Figure 6a,d,g, resulting in a lower resistance value at the HRS (Figure 4a).

Reliability Behaviors. Figure 7a,b shows the retention properties of the Ag-EMCs with different SBEs of TLG on the contact metals at 25 and 55 $^{\circ}\text{C}$, respectively. The resistance at the LRS and HRS was measured at a 0.2 V reading voltage. For the r-TLG/Ir sample, even though the retention time of more than 10^4 s is obtained, the resistance ratio is too small to be identified by the sensing circuit. Furthermore, at the elevated

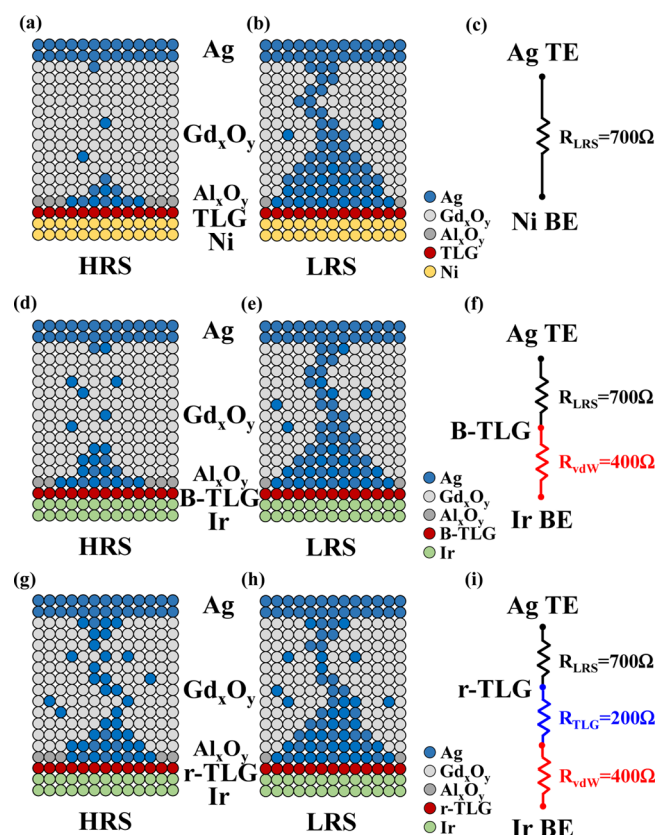


Figure 6. Illustration of the RS mechanisms of the TLG/Ni sample at the (a) HRS and (b) LRS, the B-TLG/Ir sample at the (d) HRS and (e) LRS, and the r-TLG/Ir sample at the (g) HRS and (h) LRS. The equivalent circuit diagrams of all samples at the LRS are shown in (c,f,i).

measurement temperature of 55 $^{\circ}\text{C}$, there is a retention degradation at the HRS after the retention time of 3500 s. The worse retention behavior of the r-TLG/Ir sample can be ascribed to the insufficient reset process discussed above, inducing the regeneration of the Ag filament during the retention test. Besides, the data retention characteristics of the TLG/Ni sample measured at elevated temperatures were examined and are shown in Figure 7c. We can observe that the TLG/Ni sample can maintain the resistance values at the HRS and LRS without any degradation for 10^4 s even at a measurement temperature of 115 $^{\circ}\text{C}$. Figure 7d shows the cycling test of the Ag-EMCs with different SBEs of TLG on the contact metals. Compared to the early failure of the B-TLG/Ir and r-TLG/Ir samples, the TLG/Ni sample can sustain a resistance ratio of approximately 3 orders of magnitude between HRS and LRS after operating for more than 250 cycles.

CONCLUSIONS

In this study, the Ag-EMCs with B- and r-TLG on the Ni and Ir films as BE were developed. The B- and r-TLG sheets on the Ni and Ir films can be identified using Raman mapping and AFM analyses. By examining the I – V curves, the conductive mechanism of the Ag-EMCs with the stacked BE of r-TLG on the Ir film at both HRS and LRS under a positive TE bias is found to be Schottky emission because of the existence of the energy gap of r-TLG on the Ir film and the vdW gap between the r-TLG and the Ir interface. Hence, an effective electron

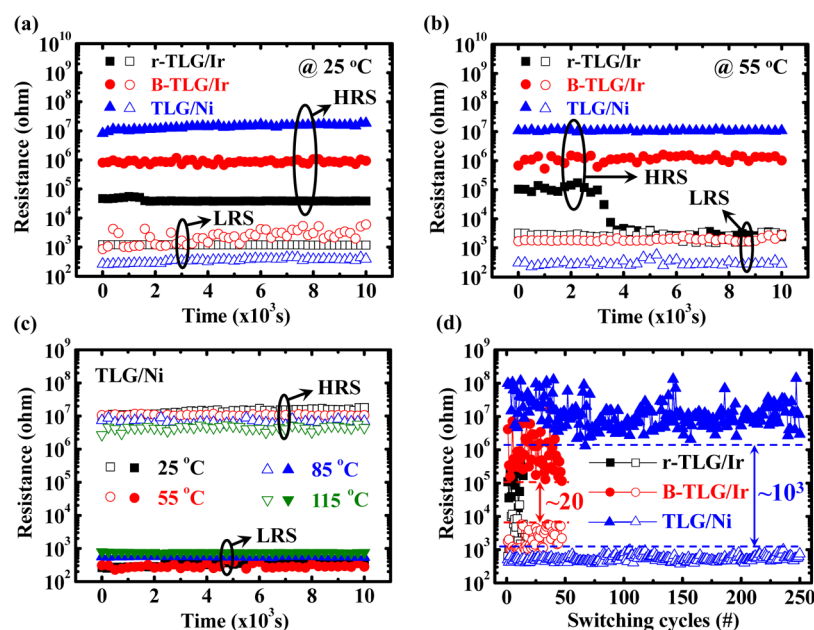


Figure 7. Data retention characteristics of the Ag-EMCs with different SBEs of TLG on the contact metals at (a) room temperature and (b) 55 °C. The resistance at the LRS and HRS was measured at a 0.2 V reading voltage. The data retention characteristics of the TLG/Ni sample measured at elevated temperatures are shown in (c). (d) Endurance characteristics of the Ag-EMCs with different SBEs of TLG on the contact metals.

barrier height of 0.262 eV at the r-TLG and Ir interface is demonstrated. To prevent the Schottky emission of TLG on the contact metals, the Ag-EMCs with TLG on the Ni film are presented to exhibit low operation voltages of +0.3 V/−0.75 V, a good endurance of more than 250 cycles, and excellent data retention for more than 10^4 s at 115 °C. The TLG sheets offer a low-power memory that can be integrated onto flexible substrates.

■ ASSOCIATED CONTENT

■ Supporting Information

The Supporting Information is available free of charge on the ACS Publications website at DOI: 10.1021/acsami.7b10407.

AFM topographic and phase images of metal films and SLG and TLG sheets transferred onto the metal films; XRD analysis and Raman spectra of the Ni film and the TLG on the Ni film with and without baking; forming characteristics; I – V characteristics of r- and B-TLG on the metal films; the fitting of J – V^2 and logarithmic I – V curves at the negative TE bias of the HRS and LRS, respectively; typical I – V characteristics and statistical distributions of the operating voltages; resistances at the HRS and LRS; and resistance ratio of the Ag-EMCs with Ir- and Ni-BEs; temperature dependence of the resistance values at the LRS of the TLG/Ni sample; a table summarizing the conductive mechanisms of all samples at positive and negative TE biases of the HRS and LRS; and the operation currents, voltages, and powers of the Ag-EMCs with different SBEs of TLG on the contact metals at set and reset processes (Figures S1–S8 and Tables S1–S2) (PDF)

■ AUTHOR INFORMATION

Corresponding Authors

*E-mail: jcwang@mail.cgu.edu.tw. Phone: +886-3-2118800 ext. 5784. Fax: +886-3-2118507 (J.-C.W.).

*E-mail: csalai@mail.cgu.edu.tw. Phone: +886-3-2118800 ext. 5786. Fax: +886-3-2118507 (C.-S.L.).

ORCID

Jer-Chyi Wang: 0000-0002-1308-3197

Notes

The authors declare no competing financial interest.

■ ACKNOWLEDGMENTS

This research was supported by the Ministry of Science and Technology, R.O.C (contract nos. of MOST 103-2221-E-182-061-MY3, MOST 105-2628-E-182-001-MY3, and MOST 105-2632-E-182-001) and Chang Gung Memorial Hospital, Linkou, Taiwan (contract nos. of CMRPD2F0121, CMRPD2F0122, and BMRPA74).

■ REFERENCES

- (1) Zhang, G.; Wang, X.-P.; Won, J. Y.; Li, M.-F. Spatial Distribution of Charge Traps in a SONOS-Type Flash Memory Using a High- k Trapping Layer. *IEEE Trans. Electron Devices* **2007**, *54*, 3317–3324.
- (2) Lu, C.-Y.; Hsieh, K.-Y.; Liu, R. Future Challenges of Flash Memory Technologies. *Microelectron. Eng.* **2009**, *86*, 283–286.
- (3) Liu, L.; Chen, B.; Gao, B.; Zhang, F.; Chen, Y.; Liu, X.; Wang, Y.; Han, R.; Kang, J. Engineering Oxide Resistive Switching Materials for Memristive Device Application. *Appl. Phys. A* **2011**, *102*, 991–996.
- (4) Wang, J.-C.; Hsu, C.-H.; Ye, Y.-R.; Lai, C.-S.; Ai, C.-F.; Tsai, W.-F. High-Performance Multilevel Resistive Switching Gadolinium Oxide Memristors with Hydrogen Plasma Immersion Ion Implantation Treatment. *IEEE Electron Device Lett.* **2014**, *35*, 452–454.
- (5) Jacob, M. V.; Taguchi, D.; Iwamoto, M.; Bazaka, K.; Rawat, R. S. Resistive Switching in Graphene-Organic Device: Charge Transport Properties of Graphene-Organic Device Through Electric Field Induced Optical Second Harmonic Generation and Charge Modulation Spectroscopy. *Carbon* **2017**, *112*, 111–116.
- (6) Egorov, K. V.; Kuzmichev, D. S.; Chizhov, P. S.; Lebedinskii, Y. Y.; Hwang, C. S.; Markeev, A. M. In Situ Control of Oxygen Vacancies in TaO_x Thin Films via Plasma-Enhanced Atomic Layer Deposition for Resistive Switching Memory Applications. *ACS Appl. Mater. Interfaces* **2017**, *9*, 13286–13292.

- (7) Azzaz, M.; Benoist, A.; Vianello, E.; Garbin, D.; Jalaguier, E.; Cagli, C.; Charpin, C.; Bernasconi, S.; Jeannot, S.; Dewolf, T.; Audoit, G.; Guedj, C.; Denorme, S.; Candelier, P.; Fenouillet-Beranger, C.; Perniola, L. Improvement of Performances HfO₂-Based RRAM From Elementary Cell to 16 kb Demonstrator by Introduction of Thin Layer of Al₂O₃. *Solid-State Electron.* **2016**, *125*, 182–188.
- (8) Wang, J.-C.; Hsu, C.-H.; Ye, Y.-R.; Ai, C.-F.; Tsai, W.-F. Performance Improvement of Gadolinium Oxide Resistive Random Access Memory Treated by Hydrogen Plasma Immersion Ion Implantation. *J. Vac. Sci. Technol., A* **2014**, *32*, 02B108.
- (9) Sawa, A. Resistive Switching in Transition Metal Oxides. *Mater. Today* **2008**, *11*, 28–36.
- (10) Menzel, S.; Tappertzhofen, S.; Waser, R.; Valov, I. Switching Kinetics of Electrochemical Metallization Memory Cells. *Phys. Chem. Chem. Phys.* **2013**, *15*, 6945–6952.
- (11) Wang, J.-C.; Chiu, C.-H.; Chen, W.-F. Thickness-Optimized Multilevel Resistive Switching of Silver Programmable Metallization Cells with Stacked SiO_x/SiO₂ Solid Electrolytes. *IEEE Trans. Electron Devices* **2015**, *62*, 1478–1483.
- (12) Haemori, M.; Nagata, T.; Chikyow, T. Impact of Cu Electrode on Switching Behavior in a Cu/HfO₂/Pt Structure and Resultant Cu Ion Diffusion. *Appl. Phys. Express* **2009**, *2*, 061401.
- (13) Chen, Y. Y.; Pourtois, G.; Adelmann, C.; Goux, L.; Govoreanu, B.; Degreave, R.; Jurczak, M.; Kittl, J. A.; Groeseneken, G.; Wouters, D. J. Insights into Ni-Filament Formation in Unipolar-Switching Ni/HfO₂/TiN Resistive Random Access Memory Device. *Appl. Phys. Lett.* **2012**, *100*, 113513.
- (14) Kozicki, M. N.; Balakrishnan, M.; Gopalan, C.; Ratnakumar, C.; Mitkova, M. Programmable metallization cell memory based on Ag-Ge-S and Cu-Ge-S solid electrolytes, *Non-Volatile Memory Technology Symposium 2005*, Dallas, Nov 7–10, 2005; pp 83–89.
- (15) Geim, A. K. Graphene: Status and Prospects. *Science* **2009**, *324*, 1530–1534.
- (16) Pacilé, D.; Meyer, J. C.; Girit, Ç. Ö.; Zettl, A. The Two-Dimensional Phase of Boron Nitride: Few-Atomic-Layer Sheets and Suspended Membranes. *Appl. Phys. Lett.* **2008**, *92*, 133107.
- (17) Wang, H.; Yuan, H.; Hong, S. S.; Li, Y.; Cui, Y. Physical and Chemical Tuning of Two-Dimensional Transition Metal Dichalcogenides. *Chem. Soc. Rev.* **2015**, *44*, 2664–2680.
- (18) Schwierz, F. Graphene Transistors. *Nat. Nanotechnol.* **2010**, *5*, 487–496.
- (19) Di Bartolomeo, A. Graphene Schottky Diodes: An Experimental Review of the Rectifying Graphene/Semiconductor Heterojunction. *Phys. Rep.* **2016**, *606*, 1–58.
- (20) Wang, J.-C.; Chang, K.-P.; Lin, C.-T.; Su, C.-Y.; Güneş, F.; Boutchich, M.; Chen, C.-H.; Chen, C.-H.; Chen, C.-S.; Li, L.-J.; Lai, C.-S. Integration of Ammonia-Plasma-Functionalized Graphene Nanodiscs as Charge Trapping Centers for Nonvolatile Memory Applications. *Carbon* **2017**, *113*, 318–324.
- (21) Bonaccorso, F.; Sun, Z.; Hasan, T.; Ferrari, A. C. Graphene Photonics and Optoelectronics. *Nat. Photonics* **2010**, *4*, 611–622.
- (22) Liu, C.; Yu, Z.; Neff, D.; Zhamu, A.; Jang, B. Z. Graphene-Based Supercapacitor with an Ultrahigh Energy Density. *Nano Lett.* **2010**, *10*, 4863–4868.
- (23) Nair, R. R.; Blake, P.; Grigorenko, A. N.; Novoselov, K. S.; Booth, T. J.; Stauber, T.; Peres, N. M. R.; Geim, A. K. Fine Structure Constant Defines Visual Transparency of Graphene. *Science* **2008**, *320*, 1308.
- (24) Suk, J. W.; Kitt, A.; Magnuson, C. W.; Hao, Y.; Ahmed, S.; An, J.; Swan, A. K.; Goldberg, B. B.; Ruoff, R. S. Transfer of CVD-Grown Monolayer Graphene onto Arbitrary Substrates. *ACS Nano* **2011**, *5*, 6916–6924.
- (25) Chen, Y.; Gong, X.-L.; Gai, J.-G. Progress and Challenges in Transfer of Large-Area Graphene Films. *Adv. Sci.* **2016**, *3*, 1500343.
- (26) Tian, H.; Zhao, H.; Wang, X.-F.; Xie, Q.-Y.; Chen, H.-Y.; Mohammad, M. A.; Li, C.; Mi, W.-T.; Bie, Z.; Yeh, C.-H.; Yang, Y.; Wong, H.-S. P.; Chiu, P.-W.; Ren, T.-L. In Situ Tuning of Switching Window in a Gate-Controlled Bilayer Graphene-Electrode Resistive Memory Device. *Adv. Mater.* **2015**, *27*, 7767–7774.
- (27) Jang, B. C.; Seong, H.; Kim, J. Y.; Koo, B. J.; Kim, S. K.; Yang, S. Y.; Im, S. G.; Choi, S.-Y. Ultra-Low Power, Highly Uniform Polymer Memory by Inserted Multilayer Graphene Electrode. *2D Mater.* **2015**, *2*, 044013.
- (28) Yang, Y.; Lee, J.; Lee, S.; Liu, C.-H.; Zhong, Z.; Lu, W. Oxide Resistive Memory with Functionalized Graphene as Built-In Selector Element. *Adv. Mater.* **2014**, *26*, 3693–3699.
- (29) Bao, W.; Jing, L.; Velasco, J., Jr.; Lee, Y.; Liu, G.; Tran, D.; Standley, B.; Aykol, M.; Cronin, S. B.; Smirnov, D.; Koshino, M.; McCann, E.; Bockrath, M.; Lau, C. N. Stacking-Dependent Band Gap and Quantum Transport in Trilayer Graphene. *Nat. Phys.* **2011**, *7*, 948–952.
- (30) Allain, A.; Kang, J.; Banerjee, K.; Kis, A. Electrical Contacts to Two-Dimensional Semiconductors. *Nat. Mater.* **2015**, *14*, 1195–1205.
- (31) Stokbro, K.; Engelund, M.; Blom, A. Atomic-Scale Model for the Contact Resistance of the Nickel-Graphene Interface. *Phys. Rev. B: Condens. Matter Mater. Phys.* **2012**, *85*, 165442.
- (32) Bertolazzi, S.; Krasnozhan, D.; Kis, A. Nonvolatile Memory Cells Based on MoS₂/Graphene Heterostructures. *ACS Nano* **2013**, *7*, 3246–3252.
- (33) Brako, R.; Šokčević, D.; Lazić, P.; Atodiresei, N. Graphene on the Ir(111) Surface: From van der Waals to Strong Bonding. *New J. Phys.* **2010**, *12*, 113016.
- (34) Huang, B.; Koh, Y. K. Improved Topological Conformity Enhances Heat Conduction Across Metal Contacts on Transferred Graphene. *Carbon* **2016**, *105*, 268–274.
- (35) Piazza, A.; Giannazzo, F.; Buscarino, G.; Fisichella, G.; La Magna, A.; Roccaforte, F.; Cannas, M.; Gelardi, F. M.; Agnello, S. Graphene p-Type Doping and Stability by Thermal Treatments in Molecular Oxygen Controlled Atmosphere. *J. Phys. Chem. C* **2015**, *119*, 22718–22723.
- (36) Dueñas, S.; Castán, H.; García, H.; Gómez, A.; Bailón, L.; Kukli, K.; Hatanpää, T.; Lu, J.; Ritala, M.; Leskelä, M. Electrical Properties of Atomic-Layer-Deposited Thin Gadolinium Oxide High-k Gate Dielectrics. *J. Electrochem. Soc.* **2007**, *154*, G207–G214.
- (37) Santos, E. J. G.; Kaxiras, E. Electric-Field Dependence of the Effective Dielectric Constant in Graphene. *Nano Lett.* **2013**, *13*, 898–902.
- (38) Chen, S.-C.; Chang, T.-C.; Chen, S.-Y.; Li, H.-W.; Tsai, Y.-T.; Chen, C.-W.; Sze, S. M.; Yeh, F.-S.; Tai, Y.-H. Carrier Transport and Multilevel Switching Mechanism for Chromium Oxide Resistive Random-Access Memory. *Electrochem. Solid-State Lett.* **2011**, *14*, H103–H106.
- (39) Wang, J.-C.; Ye, Y.-R.; Lai, C.-S.; Lin, C.-T.; Lu, H.-C.; Wu, C.-I.; Wang, P.-S. Characterization of Gadolinium Oxide Thin Films with CF₄ Plasma Treatment for Resistive Switching Memory Applications. *Appl. Surf. Sci.* **2013**, *276*, 497–501.
- (40) Bertolazzi, S.; Krasnozhan, D.; Kis, A. Nonvolatile Memory Cells Based on MoS₂/Graphene Heterostructures. *ACS Nano* **2013**, *7*, 3246–3252.
- (41) Xu, R.; Yin, L.-J.; Qiao, J.-B.; Bai, K.-K.; Nie, J.-C.; He, L. Direct Probing of the Stacking Order and Electronic Spectrum of Rhombohedral Trilayer Graphene with Scanning Tunneling Microscopy. *Phys. Rev. B: Condens. Matter Mater. Phys.* **2015**, *91*, 035410.
- (42) Zheng, J.; Wang, Y.; Wang, L.; Quhe, R.; Ni, Z.; Mei, W.-N.; Gao, Z.; Yu, D.; Shi, J.; Lu, J. Interfacial Properties of Bilayer and Trilayer Graphene on Metal Substrates. *Sci. Rep.* **2013**, *3*, 2081.
- (43) Chan, Y.-T.; Chen, W.-F.; Wang, J.-C.; Lai, C.-S. Effects of Bottom Electrode on Resistive Switching of Silver Programmable Metallization Cells with Gd_xO_y/Al_xO_y Solid Electrolytes. *Vacuum* **2017**, *140*, 30–34.
- (44) Kim, S.; Cho, S.; Park, B.-G. Effect of Bottom Electrode on Resistive Switching Voltages in Ag-Based Electrochemical Metallization Memory Device. *J. Semicond. Technol. Sci.* **2016**, *16*, 147–152.
- (45) Schindler, C.; Staikov, G.; Waser, R. Electrode Kinetics of Cu–SiO₂-Based Resistive Switching Cells: Overcoming the Voltage-Time Dilemma of Electrochemical Metallization Memories. *Appl. Phys. Lett.* **2009**, *94*, 072109.

(46) Weast, R. C. *CRC Handbook of Chemistry and Physics*, 69th ed.; CRC Press: Boca Raton, FL, 1988.